



Publication Year	2016
Acceptance in OA@INAF	2021-03-15T16:02:16Z
Title	X-RAY IRRADIATION OF H ₂ O + CO ICE MIXTURES WITH SYNCHROTRON LIGHT
Authors	JIMENEZ ESCOBAR, Antonio; Chen, Y.-J.; CIARAVELLA, Angela; Huang, C.-H.; MICELA, Giuseppina; et al.
DOI	10.3847/0004-637X/820/1/25
Handle	http://hdl.handle.net/20.500.12386/30712
Journal	THE ASTROPHYSICAL JOURNAL
Number	820

X-RAY IRRADIATION OF H₂O + CO ICE MIXTURES WITH SYNCHROTRON LIGHTA. JIMÉNEZ-ESCOBAR¹, Y.-J. CHEN², A. CIARAVELLA¹, C.-H. HUANG², G. MICELA¹, AND C. CECCHI-PESTELLINI¹¹ INAF–Osservatorio Astronomico di Palermo, P.za Parlamento 1, I-90134 Palermo, Italy;

jimenez@astropa.inaf.it, ciarave@astropa.inaf.it, giusi@astropa.inaf.it, cecchi-pestellini@astropa.inaf.it

² Department of Physics, National Central University, Jhongli District, Taoyuan City 32054, Taiwan; asperchen@phy.ncu.edu.tw, 101222023@cc.ncu.edu.tw

Received 2015 May 15; accepted 2016 February 1; published 2016 March 14

ABSTRACT

We irradiated a (4:1) mixture of water and carbon monoxide with soft X-rays of energies up to 1.2 keV. The experiments were performed using the spherical grating monochromator beamline at National Synchrotron Radiation Research Center in Taiwan. Both monochromatic (300 and 900 eV) and broader energy fluxes (250–1200 eV) were employed. During the irradiation, the H₂O + CO mixture was ionized, excited, and fragmented, producing a number of reactive species. The composition of the ice has been monitored throughout both the irradiation and warm-up phases. We identified several products, which can be related through a plausible chemical reaction scheme. Such chemistry is initiated by the injection of energetic photoelectrons that produce multiple ionization events generating a secondary electron cascade. The results have been discussed in light of a model for protoplanetary disks around young solar-type stars.

Key words: astrochemistry – ISM: molecules – methods: laboratory: molecular – molecular processes

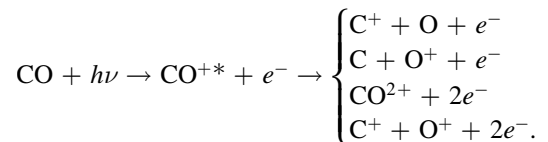
1. INTRODUCTION

The irradiation of molecules in condensed water is an important process in the chemistry of a wide variety of astronomical environments, from the cold interstellar medium to comet comae. An important component of interstellar ices is carbon monoxide, and consequently, a number of experiments have been performed in mixtures of such species with water, exploiting far (Watanabe & Kouchi 2002) and extreme-ultraviolet photons (Wu et al. 2003), energetic electrons (Bennett et al. 2011), protons (Moore & Khanna 1991), and heavy ions (de Barros et al. 2012). When subjected to ionizing radiation, water molecules are ready sources of hydrogen atoms, OH radicals, H₂O⁺, and electrons, which give rise to a wealth of chemical processes, such as protonation, OH addition, and electron reduction.

In this work we present a set of experiments in which condensed mixtures of water and carbon monoxide have been irradiated with soft X-rays. Our study is motivated by the wealth of data about young solar-type stars. It is now clear that the primordial Sun must have been much more active than today (Ribas et al. 2005) and emitted copious amounts of energetic radiation, especially in the form of intense daily or weekly flares. X-ray and UV emissions both fade with age, but the X-ray spectrum varies much more rapidly than UV, with the extent of variations depending on the hardness of radiation: the hardest the fastest. According to the study of solar-type stars of the Pleiades cluster, in the 1–10 keV range, X-ray photons at Earth were three orders of magnitude higher than today when the Sun was only 100 Myr old (Micela 2002). Such a copious energy injection must have played an important role in the chemistry of the circumsolar environment, but so far it has been quite unexplored.

The effects of X-rays on ices start with the photon absorption by parent molecules, which lead to the fragmentation of the molecules. During solid water irradiation with photons close to the O edge (≈ 540 eV), Mase et al. (1998) found that resonant absorption in the transition $4a_1 \leftarrow O(1s)$ leads to H⁺ desorption, $H_2O + h\nu \rightarrow H_2O^{++} + e^- \rightarrow OH + H^+ + e^-$. Upon resonant photoexcitation of the carbon and oxygen core

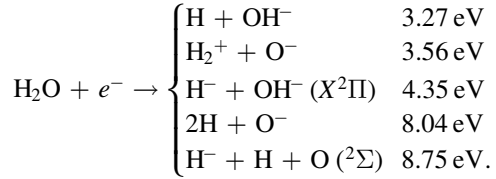
electrons, the CO molecule is fragmented into the following channels (Benndor et al. 1999):



In general, the fragmentation events are induced by the ionization or excitation of an inner-shell electron followed by either normal or resonant Auger decays, with the normal Auger decay active above the ionization threshold. The injection of energetic photoelectrons produces multiple ionization events generating a secondary electron cascade that dominates the chemistry. Impact ionizations of water and carbon monoxide are the major loss channels for photoelectrons with energies larger than few tens of eV.

There is an extensive literature for electron impact ionizations for simple molecules in different phases with the values of the absolute cross sections around a few Å², e.g., Hudson et al. (2004) for carbon monoxide (and CO₂) and Joshipura et al. (2007) for water. The latter authors estimate that electron impact ionizations are more efficient in ice than in the liquid phase, with the total ionization cross sections being larger by a factor of 2. The total ionization cross sections have a threshold around 20 eV and show a broad maximum at approximately 100 eV, and then they decline to reach roughly their values at the threshold around 1 keV. In the gas phase, carbon monoxide ionization leads preferentially to the production of CO⁺. Other ionization pathways, such as dissociations providing the formation of C⁺ and O⁺ (C⁺ favored), and double CO ionization are one and two orders of magnitude slower (Mangan et al. 2000). Water vapor molecules are ionized, producing H₂O⁺ molecular ions and to a lesser extent OH⁺ (Itikawa & Mason 2005). Other minor channels are the production of O⁺, O²⁺, H₂⁺, and H⁺. Electron impacts with the expected major product CO₂ produce CO₂⁺, CO⁺, O⁺, C⁺, O²⁺, and C²⁺, the main outcomes being CO₂⁺ and O⁺ (Itikawa 2002).

As electrons degrade their energies through subsequent ionization events, they eventually become unable to produce further ionizations and start to interact with molecules either via excitation impacts and through dissociative electron attachment (DEA), a process in which a molecule captures a low-energy electron in an excited resonant state, eventually ending up in the fragmentation of the molecular anion, $AB + e^- \rightarrow AB^{*-} \rightarrow A^- + B$ (e.g., Munro et al. 2012). DEA events show narrow cross sections, which are peaked at about 10 eV for CO and at slightly lower energies, ~ 8 eV, for CO₂. Major outcomes of the dissociations are negative ions O⁻ (e.g., Rapp & Briglia 1965). DEA to water molecules proceeds through several channels with different energetic thresholds (Haxton et al. 2007),



Excitations to electronic states of the molecules can also occur, together with vibrational excitations. Liu & Victor (1994) collected a set of carbon monoxide cross sections for electron collisions. They found that electron impact excitations of electron states in CO occur at peak energies in the range 10–20 eV, the major process being the excitations to the singlet $A^1\Pi$ and triplet $a^3\Pi$ states. Electronic excitations of water take place approximately in the range 10–20 eV, but to date very little information has been reported on absolute values of the excitation cross sections of electronic states in H₂O. Finally, the most effective electron energies in vibrational excitations of CO and H₂O are 1.2–3 eV and 5–10 eV, respectively (Fridman & Kennedy 2004).

The cross sections reported above refer mainly to gas-phase measurements or theoretical predictions. The presence of close scattering sites in the condensed phase may modify the interactions between the slowing-down electron and the molecular target. Michaud et al. (2003) derived experimentally the total cross sections for 1–100 eV electron scattering in an amorphous film of water condensed at 14 K. The cross sections are extracted from an analysis of the electron energy distribution backscattered from the film. Besides elastic scattering and the excitation of various intermolecular vibrational modes, such as librations and stretching modes, the main inelastic impacts are dissociative attachment, electronic excitation, and ionization processes (see Tables 2 and 3 in Michaud et al. 2003). Below 10 eV, DEA dominates the interaction between electrons and water molecules in the ice. Thus, the excitations of water ice by low-energy electrons break bonds, leading to the formation of atomic and molecular fragment species with high reactivity, such as the OH radical and atomic hydrogen. Something similar may occur to condensed CO with the injection in the matrix of carbon and oxygen atoms, together with their ionic counterparts.

We used synchrotron light at the National Synchrotron Radiation Research Center (NSRRC) in Hsinchu, Taiwan, to irradiate our ice samples. Synchrotron sources are ideal because of their high intensity and wide wavelength coverage. Photolyzed products have been studied as functions of the photon energies. The experimental setup is illustrated in Section 2, the products of the irradiation are described in Section 3, and in the last section we discuss the ongoing

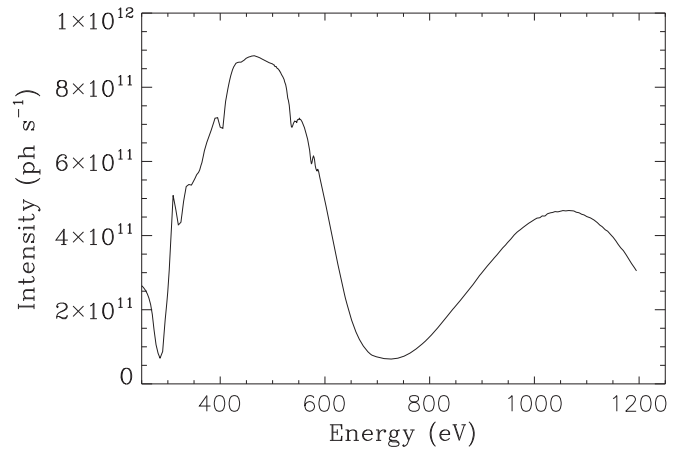


Figure 1. X-ray emission spectrum of the synchrotron radiation beam during the experiments.

chemistry and the relevance of experimental results in astrochemistry.

2. THE EXPERIMENT

The experiments have been performed with the Interstellar Photo-process System (IPS; Chen et al. 2014), an ultrahigh vacuum (UHV) chamber. The ice sample is monitored through the Fourier Transform Infrared ABB FTLA-2000-104 spectrometer equipped with a mercury-cadmium-telluride infrared detector and a Quadrupole Mass Spectrometer (QMS) covering the range of 1–200 amu (0.5 amu resolution). A detailed description of the IPS is given in Chen et al. (2014).

A base pressure of approximately 1.3×10^{-10} mbar is obtained after baking the chamber at 100°C for 48 hr. Mass spectra are recorded during the duration of the experiment in order to monitor the residual gas in the chamber and check for possible contaminations. We also check the KBr substrate by taking infrared spectra before and after cooling it at 14 K. The gas line system used to prepare the gas mixture is previously baked out at 120°C to eliminate organic and water contamination, and then we let it cool down to room temperature, reaching a base pressure lower than 1.3×10^{-7} mbar. After the deposition, the vacuum inside the chamber reaches the final base pressure in about half an hour. During this time, the conditions inside the chamber are monitored using QMS and infrared spectroscopy. Before and after irradiation, infrared spectra are collected with a resolution of 1, 2, and 4 cm⁻¹. During the experiment, the irradiation is suspended at different times to record infrared spectra with 2 cm⁻¹ resolution. At the end of the irradiation, we heat the substrate at 2 K minute⁻¹, eventually reaching room temperature. During the warm-up, infrared spectra are acquired every 10 K with a resolution of 4 cm⁻¹.

The X-ray source used in this study is the Spherical Grating Monochromator beamline at NSRRC, covering photon energies from 250 to 1250 eV. The photon flux as a function of the photon energy is shown in Figure 1. During the experiments, X-ray photon flux is monitored by an in-line nickel mesh (about 90% optical transmission), calibrated by a traceable photodiode (International Radiation Detectors, Inc.).

Table 1
Irradiation Experiments

Exp.	Energy (keV)	$N_{\text{H}_2\text{O}}$ (10^{18} cm^{-2})	N_{CO} (10^{18} cm^{-2})	Irr. Time (t_p) (minutes)	Photon Rate (photons s^{-1})	Energy Rate (eV s^{-1})	Total Absorbed Energy (eV)	X-Ray Spot Size (mm^2)
BL	blank	2.3	0.67
M3	0.3	2.3	0.63	232	1.1×10^{11}	3.5×10^{13}	3.0×10^{17}	11
M9	0.9	2.1	0.64	274	6.3×10^{11}	5.7×10^{14}	3.5×10^{18}	11
BB	0.25–1.2	2.3	0.64	60	3.7×10^{14}	3.0×10^{17}	3.0×10^{20}	24

3. RESULTS

We use a (4:1), binary mixture of water (Merck) and CO (99.999% purity, Matheson), HPLC graded and 3 times freeze-pump-thaw cycled. The set of experiments are reported in Table 1, in which for each experiment we also report the employed X-ray energies, initial H_2O and CO column densities, total irradiation times, photon and energy rates impinging on the sample, energy absorbed by the samples, and X-ray spot sizes. The infrared spot size was measured to be $A_{\text{IR}} = 50 \text{ mm}^2$ in all the experiments. The X-ray spot size, A_{X} , changes with the energy, but not with time. The 0.25–1.2 keV (hereafter broadband, BB) has the lowest infrared-to-X-ray spot size ratio ($R_g = A_{\text{IR}}/A_{\text{X}} = 2.1$), while the monochromatic fluxes at 300 (M3) and 900 eV (M9) have the same ratio ($R_g = 4.5$). An X-ray spot smaller than the infrared beam implies a dilution of the absorbance of the new species produced in the irradiated area. Thus, the computed column densities are always lower limits, with the discrepancy from the true values increasing with the infrared-to-X-ray spot size ratio. The reverse is true for parent molecules H_2O and CO. We discuss this problem in the [Appendix](#).

3.1. Irradiation

The features of H_2O and CO decrease during the irradiation, and bands associated with newly formed species appear. As an example, we report the ice infrared spectra of the BB experiment at different irradiation times in Figure 2. The irradiation with different photon fluxes leads, mainly, to the same photoproducts, with the most abundant species being carbon dioxide (CO_2). A number of additional weak features have been detected exclusively in the BB experiment. Such spectral features are attributable to carbon suboxides such as C_3O_2 and C_2O at 2196 and 2000 cm^{-1} respectively, CO_3 at 1882 cm^{-1} , C_3 at 2036 cm^{-1} , and an unidentified carrier at 2083 cm^{-1} . CO_2 was observed at the first stage of irradiation through its intense ν_3 absorption at 2342 cm^{-1} . This band is followed in intensity by the feature at 1850 cm^{-1} corresponding to a mixture of HOCO and HCO radicals (Bennett et al. 2011) appearing after 300, 60, and 30 s in M3, M9, and BB experiments, respectively.

Another “early bird” product is formaldehyde (H_2CO), identified by its features at 1716, 1498, and 1243 cm^{-1} . The strongest feature at 1716 cm^{-1} overlaps with HCOOH and the carbonic acid, H_2CO_3 (Gerakines et al. 2000), bands. In addition, HCOOH has a shoulder at 1676 cm^{-1} (Bisschop et al. 2007). The bands at 1580, 1382, and 1354 cm^{-1} are assigned to the formate ion HCOO^- (Hudson et al. 2005). The weak band at 1778 cm^{-1} was seen and reported as unidentified by Watanabe et al. (2007), and it was subsequently assigned to HOCO by Bennett et al. (2011). The band at 1098 cm^{-1} has been assigned to $(\text{CH}_2\text{OH})_2$, CH_3OCH_3 , and $\text{CH}_3\text{CH}_2\text{OH}$ by Öberg et al. (2009), who detected the feature

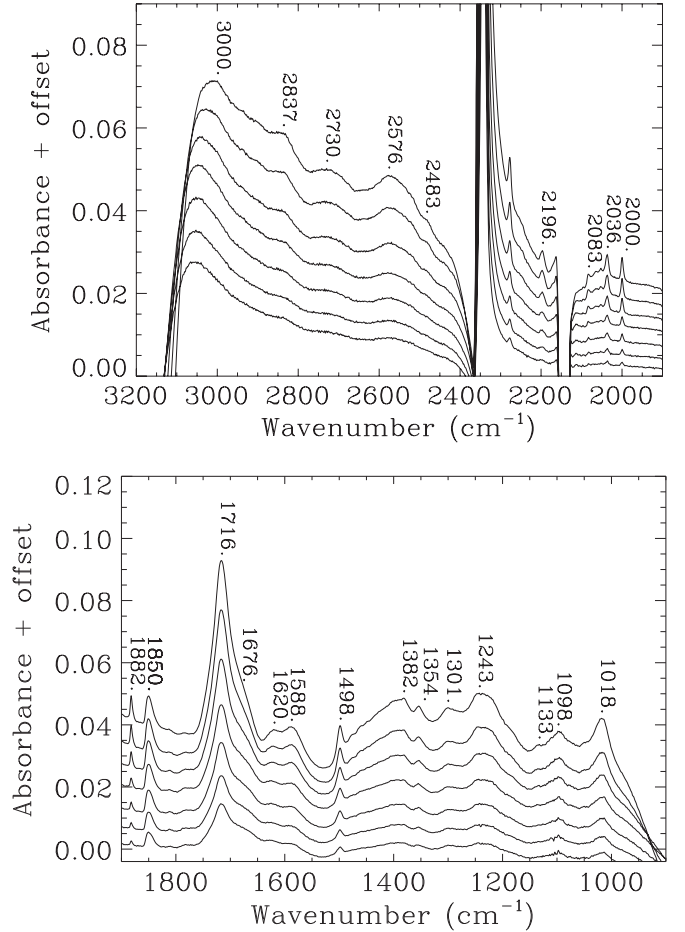


Figure 2. Infrared ice spectra taken at different irradiation times during the BB experiment as functions of the wavenumber (cm^{-1}). From bottom to top: 30, 60, 120, 210, 480, 1200, and 3600 s. The spectra are obtained by subtracting the unprocessed ice spectrum from the irradiated ones.

after ultraviolet irradiation of methanol ices. The same feature has been detected after electron irradiation of mixtures of water and carbon monoxide ices at 10 K by Bennett et al. (2011), who assigned it to the HCO radical. In fact, our data suggest multiple contributions to this feature: initially the carrier is HCO, which is one of the first products formed. In the 2400–3200 cm^{-1} region the H_2O_2 band at 2837 cm^{-1} is present, seen also after ion irradiation of thin water films (Gomis et al. 2004), in electron-irradiated crystalline water ice (Zheng et al. 2006), and UV photolysis (Cruz-Diaz et al. 2014). Finally, the post-processed irradiation spectra of (4:1) $\text{H}_2\text{O} + \text{CO}$ ice mixtures were compared with the spectrum of pure HCOOH ice taken from the Leiden database (<http://home.strw.leidenuniv.nl/~moldata/>) in Figure 3. Most of the HCOOH bands are consistent with those found in our experiments, strongly suggesting the presence of this species in the ice.

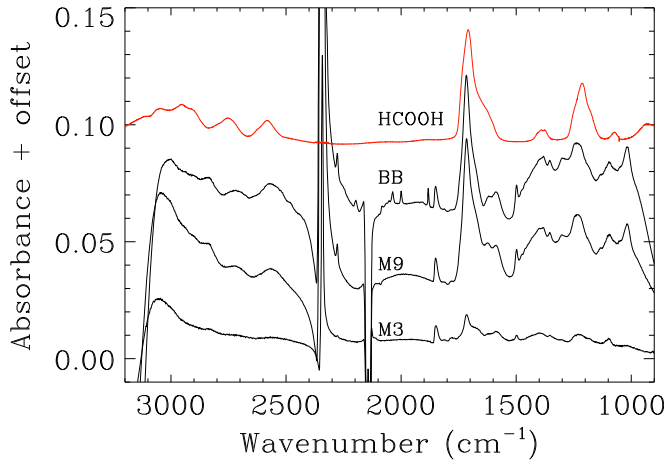


Figure 3. Comparison between the infrared spectra of (4:1) $\text{H}_2\text{O} + \text{CO}$ ice samples irradiated with different X-ray spectra (see Table 1) with the infrared signatures of pure HCOOH ice (red solid line). Formic acid data are taken from the Leiden database.

The assignment of the different molecular bands and the relative abundances with respect to CO_2 are summarized in Table 2. Final (corrected) CO_2 column densities at the end of irradiation are $N_{\text{CO}_2} = 6.8 \times 10^{16}$ (M3), 2.5×10^{17} (M9), and $2.7 \times 10^{17} \text{ cm}^{-2}$ (BB). In Tables 3–5 we report the corrected

column densities of parent molecules and products as functions of the fluence. The column densities have been computed from the absorbance integrated areas exploiting the band strengths listed in Table 2.

3.2. Warm-up and Residue of Irradiated Ices

After being irradiated, the samples are heated at a rate of 2 K minute^{-1} . We show in Figure 4 the infrared spectra during the warm-up of the ice mixture after the BB irradiation between 20–170 K (left panel) and 200–300 K (right panel). During the warm-up from 20 to 120 K, new infrared bands were observed, located at 1032, 1049, and perhaps 1070 cm^{-1} (Figure 5). Such bands appeared also during the warm-up of ices in the M9 experiment, while in the M3 experiment they were not detected. The feature that peaked at 1049 cm^{-1} desorbs at 170 K. At the same time, the peak at 1018 cm^{-1} assigned to the C–O stretching of CH_3OH (D’Hendecourt & Allamandola 1986; Gerakines et al. 1996) shifts to 1012 cm^{-1} owing to a mixing effect with the closest band at 1032 cm^{-1} ; see Figure 5. The latter could be attributed to the formation of methanol type II clathrate hydrate with water molecules (Martín-Doménech et al. 2014). An additional contribution to the 1018 cm^{-1} feature may be provided by the C–OH symmetric stretch of H_2CO_3 (Dellorusso et al. 1993). The 1049 and 1070 cm^{-1} bands are due to the formation of O_3 and CO_3 , respectively

Table 2
Identification of the Products of X-Ray Irradiation

Band (cm^{-1})	Assignment	Band Strength (cm molecule^{-1})	Fractional Column Density ^a		
			M3	M9	BB
1018	CH_3OH	1.8×10^{-17}	0.04	0.02	0.14
1098	$(\text{CH}_2\text{OH})_2$, CH_3OCH_3 , $\text{CH}_3\text{CH}_2\text{OH}$, HCO
1133 ^b	CH_3OH
1243	H_2CO , HCOOH	$(1.5\text{--}5.0) \times 10^{-17\text{c}}$	0.65–0.19	0.32–0.1	0.21–0.07
1301	CH_4	6.1×10^{-18}	0.03	0.04	0.06
1354	CH_3CHO , HCOO^-
1382 ^d	HCOO^-
1400	HCOOH , $\text{CH}_3\text{CH}_2\text{OH}$
1498	H_2CO	3.9×10^{-18}	0.23	0.13	0.12
1588	HCOO^-
1620 ^b
1676	HCOOH
1716	H_2CO , HCOOH , H_2CO_3	$6.7 \times 10^{-17\text{c}}$	0.29	0.24	0.19
1784	HOCO
1850	HCO , HOCO	$9.6 \times 10^{-18\text{e}}$	0.63	0.11	0.08
1882 ^d	CO_3	5.4×10^{-18}	0.04
2000 ^d	C_2O	2.4×10^{-17}	0.007
2036 ^d	C_3	1.0×10^{-16}	0.002
2083 ^d
2196 ^d	C_3O_2	1.3×10^{-18}	0.15
2342	CO_2	7.6×10^{-17}	1	1	1
2483 ^d
2576	HCOOH
2730	HCOOH
2837	H_2O_2	2.7×10^{-17}	0.05	0.02	0.03
3000

Notes.

^a With respect to CO_2 column density.

^b Not present in the M3 spectra.

^c HCOOH ; Bisschop et al. (2007).

^d Not present in the M3 and M9 spectra.

^e HCO ; Milligan & Jacox (1971).

Table 3
Evolution of Column Densities during the M3 Experiment

Fluence ($\times 10^{17}$ eV cm $^{-2}$)	$N(\text{CO})$ ($\times 10^{17}$ cm $^{-2}$)	$N(\text{H}_2\text{O})$ ($\times 10^{18}$ cm $^{-2}$)	$N(\text{CO}_2)$ ($\times 10^{15}$ cm $^{-2}$)	$N(\text{H}_2\text{CO})$ ($\times 10^{15}$ cm $^{-2}$)	$N(\text{HCO})$ ($\times 10^{15}$ cm $^{-2}$)
0.09	6.11(0.73) ^a	2.19(0.13)	3.69(2.14)	0.49(3.94)	0.75(1.16)
0.36	6.03(0.72)	2.16(0.13)	6.71(1.66)	1.24(3.77)	3.58(1.41)
0.94	5.96(0.61)	2.14(0.13)	9.69(1.51)	0.36(2.99)	5.94(1.19)
1.79	5.92(0.60)	2.12(0.13)	9.55(1.76)	1.25(2.21)	6.66(1.98)
1.89	5.80(0.52)	2.08(0.13)	15.28(2.30)	2.46(2.01)	10.88(1.65)
9.82	5.42(0.49)	1.96(0.12)	27.40(3.91)	7.54(1.33)	24.77(2.48)
21.14	5.00(0.23)	1.83(0.12)	44.26(6.45)	14.25(8.32)	38.97(4.14)
43.80	4.46(0.41)	1.67(0.11)	67.97(8.37)	26.63(7.18)	53.90(3.89)

Note.

^a The statistical error is given in parentheses.

Table 4
Evolution of Column Densities during the M9 Experiment

Fluence ($\times 10^{18}$ eV cm $^{-2}$)	$N(\text{CO})$ ($\times 10^{17}$ cm $^{-2}$)	$N(\text{H}_2\text{O})$ ($\times 10^{18}$ cm $^{-2}$)	$N(\text{CO}_2)$ ($\times 10^{16}$ cm $^{-2}$)	$N(\text{H}_2\text{CO})$ ($\times 10^{16}$ cm $^{-2}$)	$N(\text{HCO})$ ($\times 10^{16}$ cm $^{-2}$)
0.31	6.06(0.57) ^a	2.01(0.10)	1.83(0.21)	0.02(0.48)	1.05(0.26)
1.32	5.60(0.48)	1.87(0.10)	4.25(0.14)	0.39(0.58)	3.12(0.34)
5.23	4.73(0.40)	1.63(0.10)	9.04(0.24)	3.11(0.33)	5.91(0.26)
11.10	4.11(0.36)	1.48(0.09)	12.79(0.46)	5.05(0.48)	6.78(0.41)
27.77	3.22(0.32)	1.28(0.08)	18.74(0.85)	7.07(0.76)	7.28(0.54)
52.65	2.58(0.27)	1.14(0.08)	22.63(1.03)	8.32(0.88)	7.37(0.49)
84.44	2.16(0.24)	1.06(0.07)	25.24(1.79)	9.12(1.06)	7.20(0.50)

Note.

^a The statistical error is given in parentheses.

Table 5
Evolution of Column Densities during the BB Experiment

Fluence ($\times 10^{20}$ eV cm $^{-2}$)	$N(\text{CO})$ ($\times 10^{17}$ cm $^{-2}$)	$N(\text{H}_2\text{O})$ ($\times 10^{18}$ cm $^{-2}$)	$N(\text{CO}_2)$ ($\times 10^{16}$ cm $^{-2}$)	$N(\text{H}_2\text{CO})$ ($\times 10^{16}$ cm $^{-2}$)	$N(\text{HCO})$ ($\times 10^{16}$ cm $^{-2}$)
0.37	4.28(0.28) ^a	1.65(0.08)	11.21(0.81)	1.05(0.10)	1.49(0.12)
0.74	3.99(0.26)	1.57(0.08)	13.24(0.87)	1.48(0.21)	1.89(0.10)
1.11	3.79(0.25)	1.51(0.08)	14.37(0.88)	1.71(0.19)	2.15(0.15)
1.48	3.64(0.24)	1.48(0.08)	15.22(0.93)	1.95(0.23)	2.32(0.19)
1.86	3.52(0.24)	1.45(0.08)	15.95(0.97)	2.13(0.27)	2.44(0.20)
2.23	3.42(0.23)	1.42(0.08)	16.56(0.98)	2.33(0.31)	2.55(0.21)7
2.60	3.33(0.22)	1.40(0.08)	17.11(1.01)	2.41(0.11)	2.66(0.27)8
3.71	3.11(0.21)	1.34(0.08)	18.38(1.02)	2.78(0.32)	2.89(0.23)
5.94	2.81(0.19)	1.26(0.07)	20.13(1.07)	3.29(0.43)	3.06(0.28)
10.39	2.42(0.17)	1.16(0.07)	22.26(1.15)	3.75(0.44)	3.22(0.29)
14.84	2.20(0.15)	1.10(0.07)	23.59(1.23)	4.14(0.59)	3.23(0.30)
29.69	1.79(0.13)	0.99(0.06)	25.95(1.09)	4.61(0.52)	3.11(0.25)
44.53	1.57(0.11)	0.93(0.06)	27.12(1.13)	4.81(0.56)	2.95(0.22)

Note.

^a The statistical error is given in parentheses.

(Brewer & Wang 1972; Moll et al. 1996). The CO_3 feature at 1882 cm^{-1} disappears below 50 K.

The feature at 1850 cm^{-1} , assigned to the HCO and HOCO radicals, desorbs below 150 K (Figure 6). During warm-up, a new band at 1865 cm^{-1} shows up at approximately 60 K, reaching its maximum at 120 K. According to Gerakines et al. (1996), HCO has two features at 1850 and 1863 cm^{-1} . The appearance of this band points out that either HCO forms as the

temperature increases (with its maximum production around 120 K) or a new product is formed (probably the same kind of radical). We note that radical formation is likely to be affected by the H_2O phase transitions, reflecting differences in the porosity of the material. Water amorphous ice changes its phase (irreversibly) from high (1.1 g cm^{-3}) to low (0.94 g cm^{-3}) density between 38 and 80 K (Jenniskens et al. 1995). Such a transition increases the mobility of the radicals within the ice.

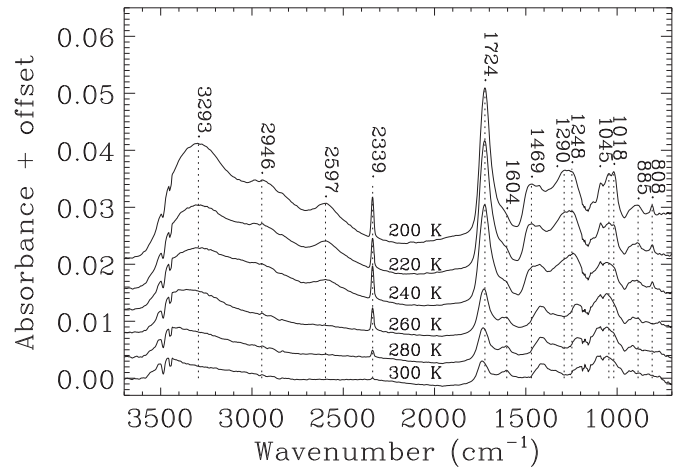
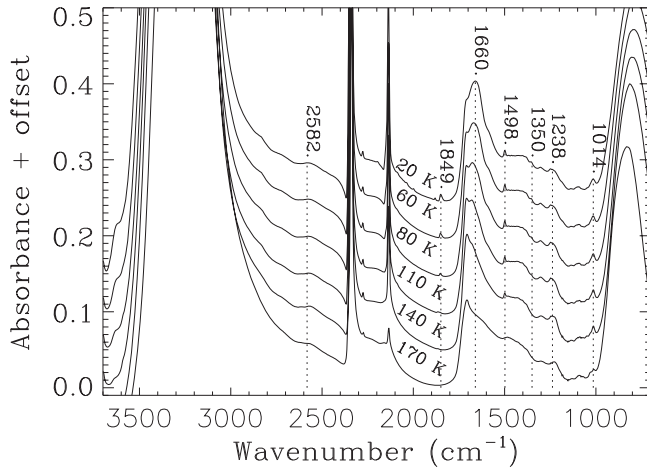


Figure 4. Infrared spectra during the warm-up of $\text{H}_2\text{O} + \text{CO}$ ice mixture after BB irradiation, in the spectral range $600\text{--}3700\text{ cm}^{-1}$. The temperature ranges from 20 to 170 K in the left panel and from 200 to 300 K in the right panel.

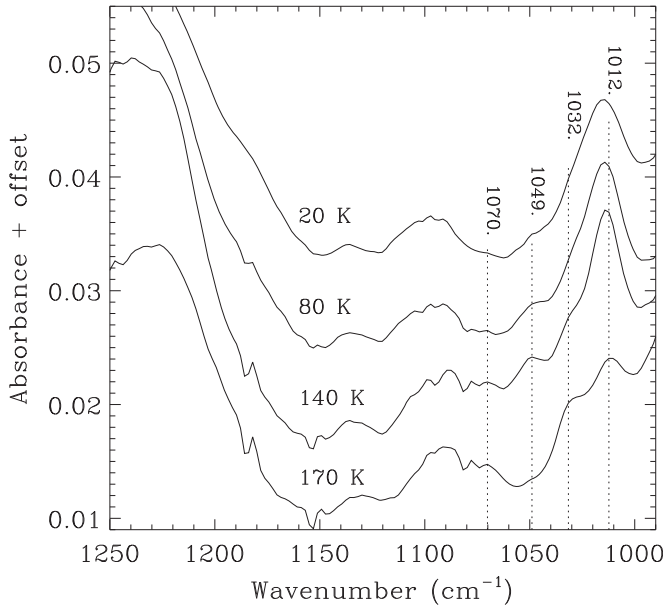


Figure 5. Infrared spectrum during the warm-up of $\text{H}_2\text{O} + \text{CO}$ ice mixture after the BB irradiation, from 20 to 170 K in the $950\text{--}1000\text{ cm}^{-1}$ spectral range.

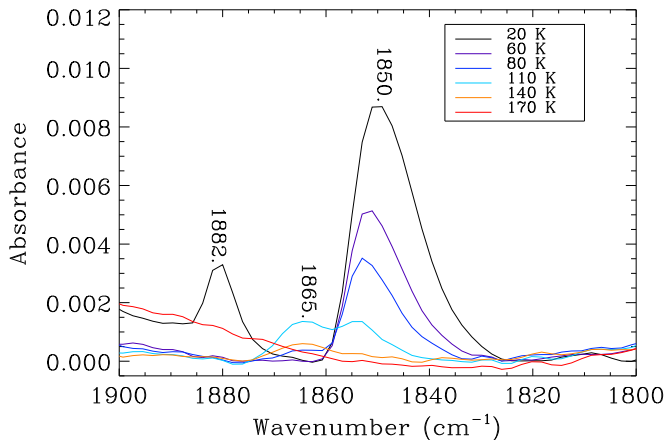


Figure 6. Infrared spectrum during the warm-up of $\text{H}_2\text{O} + \text{CO}$ ice mixture after the BB irradiation, from 20 to 170 K in the $1800\text{--}1900\text{ cm}^{-1}$ spectral range.

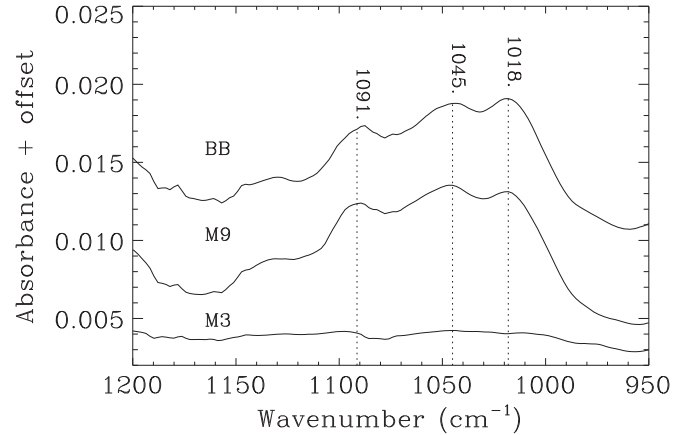


Figure 7. Infrared spectra of the irradiated ices at 200 K in the $950\text{--}1200\text{ cm}^{-1}$ range for the three experiments.

The more volatile compounds, such as HCO , H_2CO , CO , CO_2 , CH_4 , HCOOH , H_2O_2 , and carbon suboxides (formed only in the BB experiment), desorb at temperatures below water evaporation. However, a small fraction of these compounds could remain at higher temperatures trapped in the residue, and thus, e.g., the features of some volatiles like CO_2 could still be detected close to room temperature. The residual CO_2 at 200 and 300 K is roughly 1% and 0.05%, respectively, with respect to the CO_2 concentration at 14 K (the beginning of warm-up).

After water desorption, the absorption in the $3100\text{--}3500\text{ cm}^{-1}$ region is dominated by the O–H stretching (see the right panel of Figure 4). The absorption band at 2946 cm^{-1} is due to C–H stretching modes. This band, together with the $\text{—CH}_2\text{—}$ band (at 1469 cm^{-1}) and the C–O stretch ($950\text{--}1200\text{ cm}^{-1}$), supports the presence of alcohols in the residue.

Figure 7 shows the infrared spectra of irradiated ices at 200 K in the $950\text{--}1200\text{ cm}^{-1}$ region (see Table 2 for band identifications). The features displayed at 1091 and 1045 cm^{-1} are compatible with the formation of ethylene glycol (Chen et al. 2013). Moreover, a mixture of CH_3OCH_3 and $\text{CH}_3\text{CH}_2\text{OH}$ can also contribute to the band at 1091 cm^{-1} . The presence of CH_3OH at 200 K is indicated by the absorption at 1018 cm^{-1} . At 200 K the presence of HCO can be dismissed.

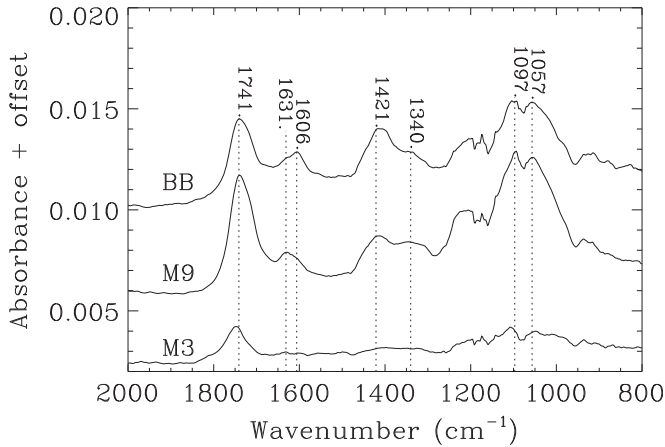


Figure 8. Infrared spectra of the residue at 300 K in the 800–2000 cm^{-1} range for the three experiments.

Finally, Figure 8 displays the residue of irradiated ices at 300 K in the 800–2000 cm^{-1} range, for the whole set of experiments. The spectra are dominated by the C=O stretching at 1741 cm^{-1} accompanied by a feature at 1421 cm^{-1} due to the aliphatic component. These bands, together with the features at 1097 and 1057 cm^{-1} (C–O stretch), confirm the presence of alcohols. The tentative identification of $(\text{CH}_2\text{OH})_2$ is suggested by the two features close to 1040 and 1090 cm^{-1} observed during the warm-up (see Figure 8). In any case the $(\text{CH}_2\text{OH})_2$ abundance cannot be large because its formation proceeds through the polymerization of CH_2OH , a direct product of methanol photolysis (Chen et al. 2013), which is not very relevant in our experiment. The infrared absorptions peaked at 1631 and 1606 cm^{-1} are characteristic of HCOOH at high temperatures. Bisschop et al. (2007) found that the feature at $\sim 1606 \text{ cm}^{-1}$ could correspond to pure HCOOH deposited at high temperature. Such a feature can be affected by the ice composition, i.e., the amount of water in the residue. The double-peak structure, displayed in M9 and BB experiments, suggests the formation of HCOOH in different hydration states. Again, M3 experiment spectra show features well embedded in the background noise.

3.3. Cross Sections for the Formation of Products

We derived the cross sections for the formation of molecular products from the strength of the infrared intensity of the spectral features associated with specific products (see Table 2), assuming a first-order kinetic process (e.g., Mennella 2010)

$$A = A_0 \times (1 - e^{-\sigma \mathcal{F}}), \quad (1)$$

where A is the feature integrated area, A_0 its asymptotic value, \mathcal{F} the fluence, and σ the cross section. For the reactants, Equation (1) is modified to (e.g., Pilling et al. 2014)

$$A = A_0 + C \times e^{-\sigma \mathcal{F}} \quad (2)$$

where $A_0 + C$ is the initial integrated area of the spectral feature. A detailed treatment can be found in e.g., Cottin et al. (2003).

The major source of error is the determination of the integrated spectral profile, due to, namely, the shape of the baseline and the spectral domain of a particular transition. The integrated absorbance of each feature was measured by integrating between baseline points on either side of the

feature. The baseline is assumed to be a linear shape underneath each feature. The integration limits are varied randomly, producing a shift and a rotation of the baseline in either direction. Results are shown in Figure 9 and Table 6 for all major species. The uncertainties of the column density given in the tables are the statistical error calculated by such systematic variation of both local baseline and integration limits.

The M3 experiment values are the most uncertain because the fluence is so low that its relation to the integrated area tends to be approximately linear. Cross sections decrease with increasing photon energies. The cross sections for the BB flux are the lowest, reflecting the general decrease of the product formation and reactant destruction in the case of very high photon fluxes (see next section and Chen et al. 2013 for the case of methanol). In addition, since cross sections depend on the energy, the results for the BB case should be sensitive to the shape of the impinging spectrum (which, however, remained constant throughout the experiments).

4. DISCUSSION

The energy absorbed by the components of an icy mixture depends on their photoabsorption cross sections and relative concentrations. In the case of our (4:1) binary mixture of H_2O and CO , we find that the ratios between the absorbed energies by water and carbon monoxide are 0.54 for the M3 experiment, 2.28 for the M9 experiment, and 1.8 for the BB experiment, respectively. At energies higher than the oxygen K edge, the ratios of C and O cross section are roughly a factor of 2, while for lower energies—as in the case of the M3 experiment—carbon dominates the photoabsorption cross section of the mixture. Such absorbed radiation ionizes and fragments the molecules; the resulting species can then diffuse and react to form new species in nonequilibrium processes.

4.1. Chemistry

Water radiolysis is well understood experimentally and theoretically in aqueous and gaseous systems (e.g., Le Caër 2011). It can be generally described as proceeding in three steps: a physical one in which the energy deposition is followed by fast relaxation processes forming mainly H_2O^+ ; a physicochemical stage with electron thermalization and ion-molecule reactions such as $\text{H}_2\text{O} + \text{H}_2\text{O}^+ \rightarrow \text{H}_3\text{O}^+ + \text{OH}^*$; and finally the chemical phase in which most reactions occur. When the process takes place in low-temperature water ice, all the interaction stages are modified, resulting in an increase of the yield of ionized states, in different decaying pathways of excited and ionized states (e.g., Kaplan & Mitrev 1987), and in the cage effect, which slows down the dissociation of molecules into radicals (e.g., Baragiola et al. 2005). In astrophysical ices the picture is further complicated by the presence of molecular species comixed with water. The short-timescale response of molecules to the initial energy deposition is very poorly known, so that most of the information relies on the product species synthesized during the much longer chemical phase. There are strong indications that water-dominated ices are excellent storage systems for stable polycyclic aromatic hydrocarbon radical cations (Gudipati & Allamandola 2006). Further experiments are required to understand if storage also occurs for other kind of organic species.

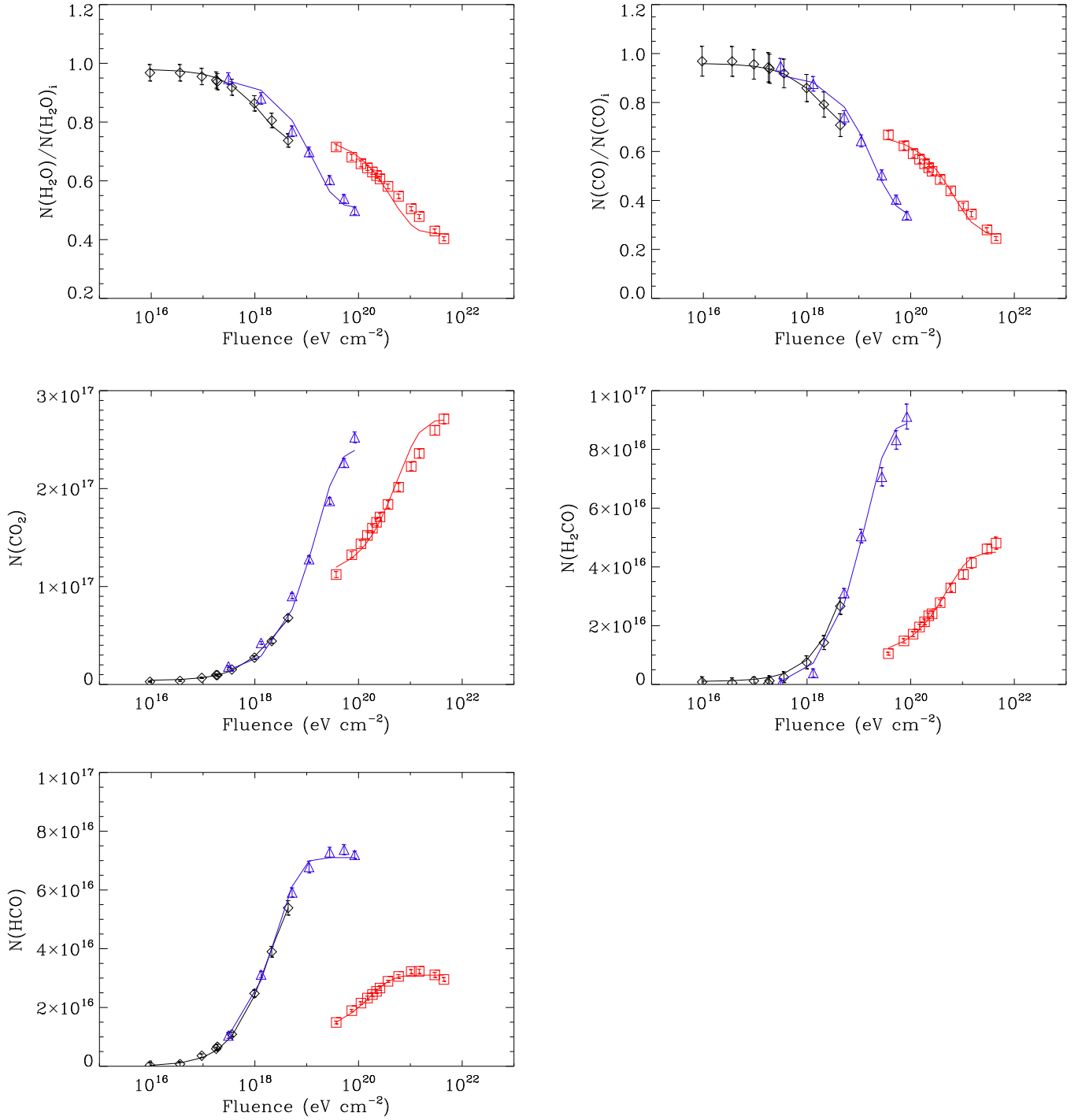


Figure 9. First-order decay fits to the H_2O , CO , CO_2 , H_2CO , and HCO column densities as functions of the X-ray fluence for the M3 (diamonds), M9 (triangles), and BB (squares) experiments. The column densities of the parent molecules are normalized to their initial values.

There exists a large body of laboratory data of the irradiation of water ice exploiting as ionizing radiation electrons, and a large range of ion energies and types (e.g., Johnson 2010). The case of X-ray irradiation has been theoretically and experimentally described by, e.g., Gullikson & Henke (1989) and recently summarized by Pilling & Bergantini (2015). The core of the process is the injection of tens of secondary electrons inside matter following the absorption of a photon. The mean free path of the secondary electrons is significantly reduced in comparison with photoelectrons so that the energy

deposition is local. The energy cascade ends up with electrons of low energy (Henke et al. 1979), which may produce further destruction in the ice through, e.g., DEA. However, detailed mechanisms of chemical reaction pathways induced by irradiation are not yet fully understood (e.g., Gudipati & Cooper 2013).

We construct a chemical scheme based on the identified products and their order of appearance. In addition to H and OH, water is a source of H_2O^+ that can easily provide H_2O_2 and H_3O^+ (e.g., Baragiola et al. 2013). Carbon dioxide,

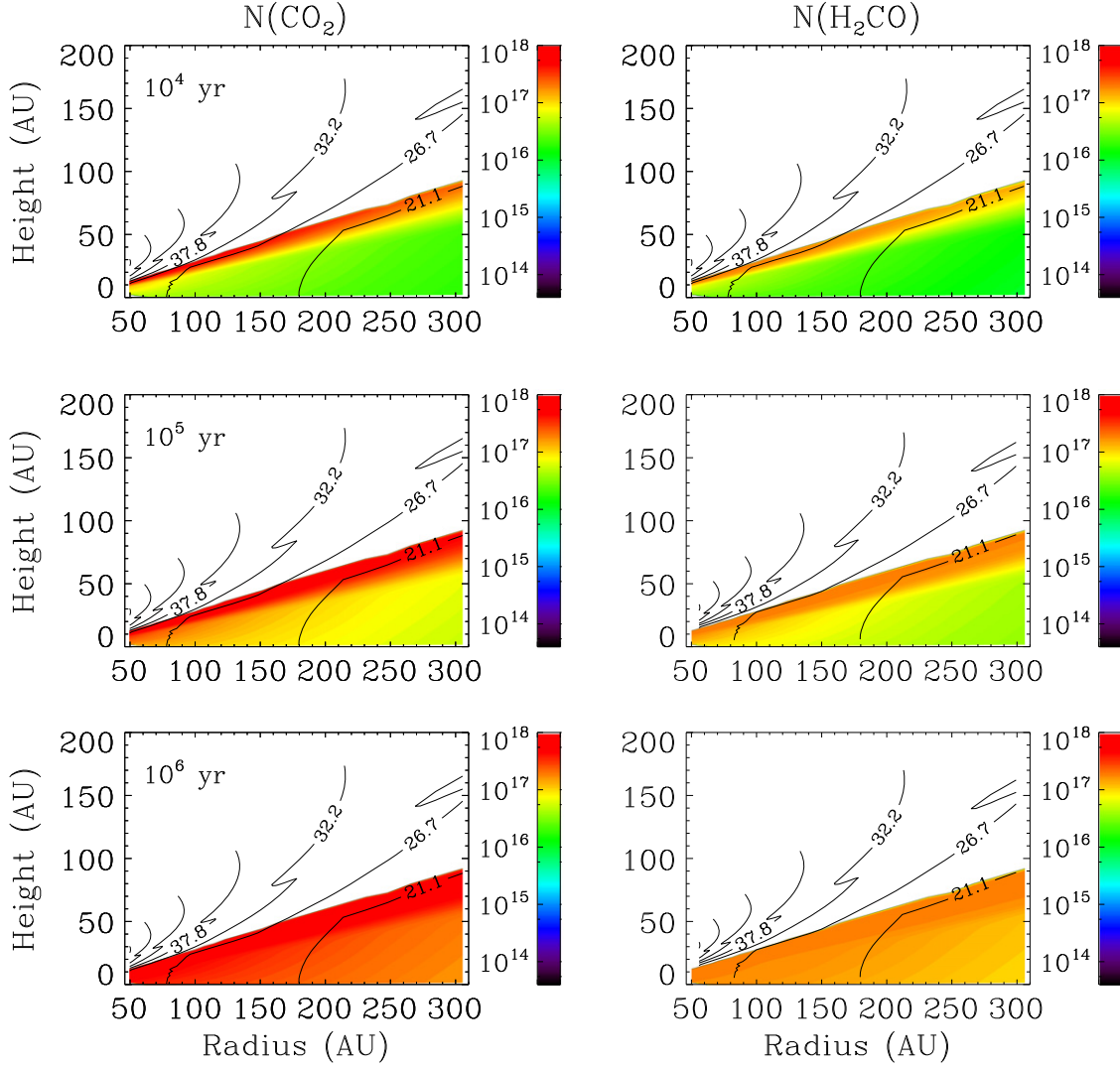


Figure 10. Chemical evolution of CO₂ (left panels) and H₂CO (right panels) column densities in a synthetic protoplanetary disk around a classical T Tauri star. Evolutionary ages, top to bottom, are 10⁴, 10⁵, and 10⁶ yr. The ice processing is entirely due to the X-ray field.

the main product, is formed through reaction of CO with atomic oxygen and OH (Watanabe & Kouchi 2002), and to a lesser extent with excited CO (Gerakines et al. 1996), where here the excitation mechanism is electron impact rather than radiation. Hydrogen addition reactions form HCO, formaldehyde, and, through CH₂OH and CH₃O, methanol. Another possible channel for methanol formation is $2 \times \text{H}_2\text{CO} \rightarrow \text{CH}_3\text{OH} + \text{CO}$. Reactions of HCO with OH are a source of HCOOH compounds that end up in HCOO⁻. From CH₃OH subsequent reactions result in further production of chemical species: e.g., methanol decomposition in CH₃ + OH produces methane through hydrogenation of CH₃. Subsequent oxydizations lead to the formation of alcohols.

As in the case of methanol ice (see Chen et al. 2013), we find a nonlinear dependence of product concentrations with flux, at very high deposition rates. This is reminiscent of the case of extreme-ultraviolet photoprocessing, in which products saturate at very high irradiation rates (e.g., Baragiola et al. 2013). It is clear from Figure 9 that M3 and M9 are in the linear flux regime, while the BB irradiation provides a lesser amount of products given the same absorbed energy. CO₂ has the final

column densities 6.8×10^{16} (M3), 2.5×10^{17} (M9), and $2.7 \times 10^{17} \text{ cm}^{-2}$ (BB). Using the total absorbed energies reported in Table 1, the corresponding final formation yields are 0.07, 0.05, and $0.0005 \text{ cm}^{-2} \text{ eV}^{-1}$, respectively. This behavior is reflected by the low values of product formation cross sections derived for the BB experiment. Nevertheless, in this experiment, although the product concentrations are saturated, the chemistry appears to be more evolved than in the M3 and M9 experiments. In other words, there are (fractionally) more end products, such as methane and methanol. At the same time, the abundance of HCO declines sharply. Such trends may suggest that a relevant fraction of the deposited energy is stored in nonchemical processes such as heating of the ice by electron-electron collisions.

The ionization rate per unit volume in the ice can be roughly estimated by means of the relation $\zeta = \Phi / (\mathcal{P}A_X) \times \eta \text{ photons cm}^{-3} \text{ s}^{-1}$, where Φ is the photon flux, \mathcal{P} the penetration length, and η the number of ionization events per photoelectron. Setting the number density of the ice in the interaction region to $N_{\text{ice}}/\mathcal{P}$ with $N_{\text{ice}} = N_{\text{H}_2\text{O}} + N_{\text{CO}}$, we obtain a fractional ionization rate $f = \Phi / (N_{\text{ice}}A_X) \times \eta \text{ s}^{-1}$.

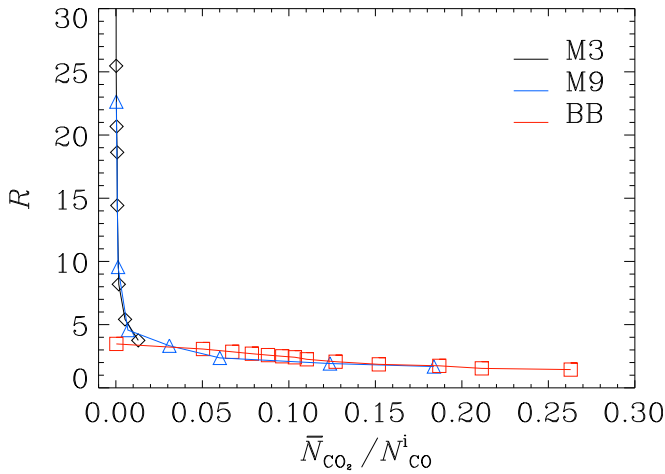


Figure 11. Correction profiles R for the M3 (black line + diamonds), M9 (blue line + triangles), and BB (red line + squares) experiments as functions of the measured CO_2 column densities.

Substituting the values reported in Table 1, and choosing the conservative value $\eta = 10$, we obtain $f = 3 \times 10^{-6}$, 2×10^{-5} , and $7 \times 10^{-3} \text{ s}^{-1}$ for the M3, M9, and BB experiments, respectively. Thus, in the BB experiments the local number of low-energy secondary electrons (per second) approaches 1% of the number of molecules. In such a scenario heating by electron–electron Coulomb interactions tends to dominate the thermal balance (see, e.g., Dalgarno et al. 1999 for a gas of solar composition). For lower fractional ionizations, as in the case of the M3 and M9 experiments, the chemistry scales linearly with the flux.

4.2. Astrophysical Implications

Walsh et al. (2010) put forward a chemical and emission model of protoplanetary disks around classical T Tauri stars, young stars that will evolve into main-sequence stars resembling our Sun. In particular, they investigated an axisymmetric region surrounding a star with mass $0.5 M_{\odot}$, radius of 2 solar radii, effective temperature of 4000 K, and $L_X = 10^{30} \text{ erg s}^{-1}$ (Walsh et al. 2012). In the model, the X-ray luminosity is taken to be constant throughout the disk evolution.

Exploiting the fitting results derived in Section 3.3, we simulate the chemical evolution of the $\text{H}_2\text{O} + \text{CO}$ ices in such a synthetic disk representation. X-rays penetrate much deeper into the disk than UV photons do. We select in the disk only the regions in which the X-ray field is 100 times or more brighter than the UV flux. This region is located in the densest and coldest (temperatures lower than 30 K) part of the disk midplane, at radii larger than 50 au. Since the M3 results are uncertain and the BB spectrum shape (see Figure 1) differs significantly from the profiles of the Walsh et al. (2012) X-ray flux (and it is possibly not relevant in the astrophysical context; see Section 4.1), we assume that the ice chemistry in the disk depends on the fluence in the same way as in the M9 experiment. In Figure 10 we show the column densities of CO_2 and H_2CO , obtained using Equation (1) at evolutionary times of 10^4 , 10^5 , and 10^6 yr, the last value being the final integration time in the Walsh et al. (2012) calculations.

With the advent of ALMA, it has been possible to constrain the relative contributions of gas-phase and icy grain-surface formation pathways of small organic molecules.

Recently, Loomis et al. (2015) derived the spatial distribution of H_2CO emission in the disk around the young low-mass star DM Tau, a classical T Tauri star of spectral type M1 and age $\sim 5 \times 10^6$ yr. Such emission is centrally peaked and extends out to ~ 500 au. Loomis et al. (2015) inferred that, while gas-phase formation accounts for the centrally peaked emission, grain-surface chemistry and desorption of H_2CO are necessary to reproduce the emission outward of the CO snowline. Our H_2CO formation rates provide H_2CO column densities that are about two orders of magnitude larger than the observed values. However, such formation efficiency cannot be directly translated into gas-phase abundances. Garrod (2013) estimates that about 10% of the grain-surface reactions result in desorption of the product, and this figure could be even lower. In addition, the X-ray luminosity of the star DM Tau is probably lower than $10^{29} \text{ erg s}^{-1}$ (Damiani et al. 1995). The column densities resulting from our experiment are thus approximately consistent with the findings of Loomis et al. (2015). Such a conclusion arises from a brutal comparison of data made without any modeling interface. Certainly, in protoplanetary disks chemistry is much more complex (e.g., Henning & Semenov 2013), particularly in the midplane, far from the protostar, in which the combination of high density and cold gas and dust induces a wealth of chemical interactions involving both gas-phase and ice species. Nevertheless, the results of our experiments imply that X-rays may induce chemical enrichment of dirty water ices in protoplanetary disks, even in the absence of other sources of energy, such as UV fields, or other chemical routes. Thus, around young solar-type stars, known to emit many more X-rays than the present-day Sun (e.g., Cecchi-Pestellini et al. 2009), X-ray irradiation has a potential role in prebiotic chemistry of those regions of disks where the material precursors of comets may be photoprocessed. While this is expected, the efficiency of X-rays in the increasing of complexity in circumstellar chemistry can hardly be overstated.

We are grateful to Dr. C. Walsh for having kindly provided us with her disk model data. We also thank the anonymous referee for her/his criticism and suggestions that helped the clarity of the manuscript. C.C.-P. acknowledges the support of the Autonomous Region of Sardinia, Project CRP 26666 (Regional Law 7/2007, Call 2010). This work was supported by the MOST grants MOST 103-2112-M-008-025-MY3 (Y.J.C.). A.J.-E., A.C., G.M., and C.C.-P. acknowledge the financial contribution from Italian MIUR through the Progetto Premiale “A way to other worlds.”

APPENDIX

In situ analyses of the processed ice sample are performed by a Fourier transform infrared spectrometer. In experiments using synchrotron light the infrared spot size (A_{IR}) is generally wider than the X-ray-illuminated area (A_X), and this discrepancy affects the determination of the column densities of both parent molecules and products. In principle, the differences in the spot sizes could be handled by using as a dilution factor the geometrical ratio $R_g = A_{\text{IR}}/A_X$. In the ideal case the relation between measured (\bar{N}_i) and “true” (N_i) column densities is given by the expression

$$R_g e^{-\sigma_i \bar{N}_i} = (R_g - 1) e^{-\sigma_i N_i^*} + e^{-\sigma_i N_i}, \quad (3)$$

Table 6
Cross Sections for Reactant Decays and Product Formations during Soft X-Ray Radiolysis of (4:1) Binary Mixtures of H₂O and CO

Mode (cm ⁻¹)	M3		M9		BB	
	Cross Section (cm ²)	Std Dev	Cross Section (cm ²)	Std Dev	Cross Section (cm ²)	Std Dev
3272 H ₂ O	6.1×10^{-19}	3.0×10^{-19}	7.6×10^{-20}	1.2×10^{-20}	2.3×10^{-21}	4.4×10^{-22}
2136 CO	4.7×10^{-19}	2.0×10^{-19}	5.2×10^{-20}	3.4×10^{-21}	1.5×10^{-21}	4.4×10^{-22}
2342 CO ₂	3.9×10^{-19}	8.2×10^{-20}	6.5×10^{-20}	2.6×10^{-21}	1.7×10^{-21}	2.5×10^{-22}
1850 HCO	5.2×10^{-19}	1.0×10^{-19}	3.7×10^{-19}	5.4×10^{-20}	6.0×10^{-21}	5.3×10^{-22}
1498 H ₂ CO	1.0×10^{-19}	1.0×10^{-20}	7.3×10^{-20}	5.8×10^{-21}	2.0×10^{-21}	1.5×10^{-22}

where σ_i is the infrared absorption cross section for the i th transition and N_i^* is the initial (before irradiation) column density. $N_i^* = 0$ for the product species, while for the parent molecules it is equal to the values reported in Table 1. In the optically thin case relation (3) reads as

$$N_i = R_g \bar{N}_i + N_i^* (1 - R_g). \quad (4)$$

Unfortunately, instrumental effects, such as nonuniform infrared illumination of the sample, make the use of the above relations impractical even in the case of optically thin transitions, leading to embarrassing cases in which, e.g., the number of atomic nuclei is not conserved.

As an example we consider the case of the optically thin 2092 cm⁻¹ transition in ¹³CO, whose optical depth is lower than 0.05. In the M9 experiment ($R_g = 4.5$), the initial and final integrated areas of this transition are ~ 0.02 and 0.01 cm⁻¹, respectively. With these values the straightforward application of relation (4) produces a negative value, i.e., a negative column density. In the same way the corrected integrated area for the 2342 cm⁻¹ transition in ¹³CO₂ (decreased by a factor of 7 to take into account the differences in the band strengths) is 0.03, larger than the initial value of ¹³CO. This suggest that correcting the data with the geometrical dilution factor leads to an overestimate of the column densities of product species.

A possible way to overcome such a problem is to constrain the correction exploiting a normalization condition in the X-ray-illuminated region, e.g., for carbon nuclei $N_{\text{CO}} + N_{\text{CO}_2} + \sum N_{\text{C}} = N_{\text{CO}}^*$, $\sum N_{\text{C}}$ being the cumulative column densities of minor carbon-bearing species. Using the measured values, this relation reads as

$$\mathcal{R}_1 \bar{N}_{\text{CO}} + \mathcal{R}_2 (\bar{N}_{\text{CO}_2} + \sum \bar{N}_{\text{C}}) = N_{\text{CO}}^* \quad (5)$$

where $\mathcal{R}_1 \leq 1$ and $\mathcal{R}_2 \geq 1$ are two correction factors depending on the measured column densities of both parent and product molecules (and thus on the irradiation time), approaching unity when $R_g \rightarrow 1$. Since product species are initially optically thin we generalize relation (2) setting $\mathcal{R}_2 = R(\bar{N}_i)$. Expanding the correction factor for the parent molecules at the second order in R^{-1} , we get $\mathcal{R}_1 = (1 - 1/R + 1/R^2)$, the first-order correction being valid only for very high spot size ratios, $R_g \gg 1$. We thus obtain a cubic equation, whose solution gives the correction profile (Figure 11) at any irradiation time.

Such a kind of “universal” correction (calibrated on C-bearing species) is of course rather approximate, overlooking, e.g., species-dependent optical depth effects. Nevertheless, it goes in the right direction, providing corrections that are a “compromise” between lower limits and the overestimating geometrical factor.

REFERENCES

- Baragiola, R. A., Famà, M. A., Loeffler, M. J., et al. 2013, in *The Science of Solar System Ices*, ed. M. S. Gudipati, & J. Castillo-Rogez (New York: Springer), 527
- Baragiola, R. A., Loeffler, M. J., Raut, U., Vidal, R. A., & Wilson, C. D. 2005, *RaPC*, **72**, 187
- Benndor, M., Westerveld, W. B., van Eck, J., van der Weg, J., & Heideman, H. G. M. 1999, *JPhB*, **32**, 2503
- Bennett, C. J., Hama, T., Kim, Y.-S., Kawasaki, M., & Kaiser, R. 2011, *ApJ*, **727**, 27
- Bisschop, S. E., Fuchs, G. W., Boogert, A. C. A., van Dishoeck, E. F., & Linnartz, H. 2007, *A&A*, **470**, 749
- Brewer, L., & Wang, J. L. 1972, *JChPh*, **56**, 759
- Cecchi-Pestellini, C., Ciaravella, A., Micela, G., & Penz, T. 2009, *A&A*, **496**, 863
- Chen, Y.-J., Chuang, K.-J., Munõz Caro, G. M., et al. 2014, *ApJ*, **781**, 15
- Chen, Y.-J., Ciaravella, A., Munõz Caro, G. M., et al. 2013, *ApJ*, **778**, 162
- Cottin, H., Moore, H. M., & Bénilan, Y. 2003, *ApJ*, **590**, 874
- Cruz-Diaz, G. A., Munõz Caro, G. M., Chen, Y.-J., & Yih, T.-S. 2014, *A&A*, **562**, A119
- Dalgarno, A., Yan, M., & Liu, W. 1999, *ApJS*, **125**, 237
- Damiani, F., Micela, G., Sciortino, S., & Harnden, F. R., Jr. 1995, *ApJ*, **446**, 331
- de Barros, A. L. F., Boduch, P., Domaracka, A., Rothard, H., & de Silveira, E. F. 2012, *LTP*, **38**, 953
- Dellorusso, N., Khanna, R. K., & Moore, M. H. 1993, *JGR*, **98**, 5505
- D’Hendecourt, L. B., & Allamandola, L. J. 1986, *A&AS*, **64**, 453
- Fridman, A., & Kennedy, L. A. 2004, *Plasma Physics and Engineering* (London: Taylor & Francis)
- Garrod, R. T. 2013, *ApJ*, **765**, 60
- Gerakines, P. A., Moore, M. H., & Hudson, R. L. 2000, *A&A*, **357**, 793
- Gerakines, P. A., Schutte, W. A., & Ehrenfreund, P. 1996, *A&A*, **312**, 289
- Gomis, O., Leto, G., & Strazzulla, G. 2004, *A&A*, **420**, 405
- Gudipati, L. S., & Allamandola, L. J. 2006, *ApJ*, **638**, 286
- Gudipati, L. S., & Cooper, P. D. 2013, in *The Science of Solar System Ices*, ed. M. S. Gudipati, & J. Castillo-Rogez (New York: Springer), 503
- Gullikson, E. M., & Henke, B. L. 1989, *PhRvB*, **39**, 1
- Haxton, D. J., McCurdy, C. W., & Rescigno, T. N. 2007, *PhRvA*, **75**, 012710
- Henke, B. L., Liesegang, J., & Smith, S. D. 1979, *PhRvB*, **19**, 30
- Henning, T., & Semenov, D. 2013, *ChRv*, **113**, 9016
- Hudson, J. E., Vallance, C., & Harland, P. W. 2004, *JPhB*, **37**, 445
- Hudson, R. L., Moore, M. H., & Cook, A. M. 2005, *ASR*, **36**, 148
- Itikawa, Y. 2002, *JPCRD*, **31**, 749
- Itikawa, Y., & Mason, N. 2005, *JPCRD*, **34**, 1
- Jenniskens, P., Blake, D. F., Wilson, M. A., & Pohorille, A. 1995, *ApJ*, **455**, 389
- Johnson, R. E. 2010, in *Physics and Chemistry at Low Temperatures*, ed. L. Khriachtchev (Singapore: World Scientific), 297
- Joshiyura, K. N., Gangopadhyay, S., Limbachiya, C. G., & Vinodkumar, M. 2007, *JPhCS*, **80**, 012008
- Kaplan, I. G., & Mitirev, A. N. 1987, *AdChP*, **68**, 255
- Le Caër, S. 2011, *Water*, **3**, 235
- Liu, W., & Victor, G. 1994, *ApJ*, **435**, 909
- Loomis, R. A., Cleaves, L. I., Öberg, K. I., Guzman, Vi. V., & Andrews, S. M. 2015, *ApJL*, **809**, L25
- Mangan, M. A., Lindsay, B. G., & Stebbings, R. F. 2000, *JPhB*, **33**, 3225
- Martín-Doménech, R., Muñoz Caro, G. M., Bueno, J., & Goesmann, F. 2014, *A&A*, **564**, A8
- Mase, K., Nagasono, M., Tanaka, S., & Urusi, T. 1998, *JChPh*, **108**, 6550
- Mennella, V. 2010, *ApJ*, **718**, 867

- Micela, G. 2002, in ASP Conf. Ser. 269, *The Evolving Sun and Its Influence on Planetary Environments*, ed. B. Montesinos, A. Gimenez, & E. F. Guinan (San Francisco, CA: ASP), 107
- Michaud, M., Wen, A., & Sanche, L. 2003, *Rad. Res.*, 159, 3
- Milligan, D. D., & Jacox, M. E. 1971, *JChPh*, 54, 927
- Moll, N. B., Ckitter, D. R., & Thompson, W. E. 1996, *JChPh*, 45, 4469
- Moore, M. H., & Khanna, R. 1991, *JGR*, 96, 17541
- Munro, J. J., Harrison, S., Fujimoto, M. M., & Tennyson, J. 2012, *JPhCS*, 388, 012013
- Öberg, K. I., Garrod, R. T., van Dishoeck, E. F., & Linnartz, H. 2009, *A&A*, 504, 891
- Pilling, S., & Bergantini, A. 2015, *ApJ*, 811, 151
- Pilling, S., Nair, P. G., Escobar, A., Frazer, H., & Mason, N. 2014, *EPJD*, 68, 58
- Rapp, D., & Briglia, D. D. 1965, *JChPh*, 43, 1480
- Ribas, I., Guinan, E. F., Gudel, M., & Audard, M. 2005, *ApJ*, 622, 680
- Walsh, C., Millar, T. J., & Nomura, H. 2010, *ApJ*, 722, 1607
- Walsh, C., Nomura, H., Millar, T. J., & Aikawa, Y. 2012, *ApJ*, 747, 114
- Watanabe, N., & Kouchi, A. 2002, *ApJ*, 567, 651
- Watanabe, N., Mouri, O., Nagaoka, A., et al. 2007, *ApJ*, 668, 1001
- Wu, R., Judge, D., Cheng, B., et al. 2003, *BAAS*, 35, 941
- Zheng, W., Jewitt, D., & Kaiser, R. I. 2006, *ApJ*, 639, 534